Atmos. Chem. Phys. Discuss., 13, 20677–20727, 2013
www.atmos-chem-phys-discuss.net/13/20677/2013/
doi:10.5194/acpd-13-20677-2013

Atmospheric Chemistry and Physics Discussions

This discussion paper is/has been under review for the journal Atmospheric Chemistry and Physics (ACP). Please refer to the corresponding final paper in ACP if available.

Secondary organic aerosol yields of 12-carbon alkanes

C. L. Loza[1], J. S. Craven[1], L. D. Yee[2], M. M. Coggon[1], R. H. Schwantes[2], M. Shiraiwa[1,3], X. Zhang[2], K. A. Schilling[1], N. L. Ng[4], M. R. Canagaratna[5], P. J. Ziemann[6], R. C. Flagan[1,2], and J. H. Seinfeld[1,2]

[1]Division of Chemistry and Chemical Engineering, California Institute of Technology, Pasadena, CA, USA
[2]Division of Engineering and Applied Science, California Institute of Technology, Pasadena, CA, USA
[3]Multiphase Chemistry Department, Max Planck Institute for Chemistry, Mainz, Germany
[4]School of Chemical and Biomolecular Engineering and School of Earth and Atmospheric Sciences, Georgia Institute of Technology, Atlanta, GA, USA
[5]Aerodyne Research, Inc., Billerica, MA, USA
[6]Air Pollution Research Center, Department of Environmental Sciences, and Environmental Toxicology Graduate Program, University of California, Riverside, CA, USA

Received: 29 June 2013 – Accepted: 26 July 2013 – Published: 7 August 2013

Correspondence to: J. H. Seinfeld (seinfeld@caltech.edu)

Published by Copernicus Publications on behalf of the European Geosciences Union.

Abstract

Secondary organic aerosol (SOA) yields were measured for cyclododecane, hexylcyclohexane, *n*-dodecane, and 2-methylundecane under high- and low-NO_x conditions, in which alkyl peroxy radicals (RO_2) react primarily with NO and HO_2, respectively, for multiple initial alkane concentrations. Experiments were run until 95–100 % of the initial alkane had reacted. Particle wall loss was evaluated as two limiting cases. SOA yield differed by 2 orders of magnitude between the two limiting cases, but the same trends among alkane precursors were observed for both limiting cases. Vapor-phase wall losses were addressed through a modeling study and increased SOA yield uncertainty by approximately 30 %. SOA yields were highest from cyclododecane under both NO_x conditions. Under high-NO_x conditions, SOA yields increased from 2-methylundecane < dodecane ~ hexylcyclohexane < cyclododecane, consistent with previous studies. Under low-NO_x conditions, SOA yields increased from 2-methylundecane ~ dodecane < hexylcyclohexane < cyclododecane. The presence of cyclization in the parent alkane structure increased SOA yields, whereas the presence of branch points decreased SOA yields due to increased vapor-phase fragmentation. Vapor-phase fragmentation was found to be more prevalent under high-NO_x conditions than under low-NO_x conditions. For different initial concentrations of the same alkane and same NO_x conditions, SOA yield did not correlate with SOA mass throughout SOA growth, suggesting kinetically limited SOA growth for these systems.

1 Introduction

Alkanes are emitted from combustion sources and can comprise up to 90 % of anthropogenic emissions in urban areas (Rogge et al., 1993; Fraser et al., 1997; Schauer et al., 1999, 2002) and 67.5 %, 56.8 % and 82.8 % of the mass of diesel fuel, liquid gasoline, and non-tailpipe gasoline sources (Gentner et al., 2012). Upon atmospheric oxidation by OH and NO_3 radicals, alkanes form lower-volatility products that can condense as secondary organic aerosol (SOA). Ambient lifetimes against reaction with OH range, for example, from 0.5 days for *n*-hexadecane to 1.4 days for *n*-octane (Atkinson and Arey, 2003; Seinfeld and Pandis, 2006), allowing for the transport of alkanes from urban to rural areas.

SOA formation under high-NO_x conditions has received much attention. Lim and Ziemann (2005, 2009a, c) developed a mechanism for linear, branched, and cyclic alkane oxidation that includes the formation of multi-generation oxidation products. SOA yields, defined as mass of SOA formed divided by mass of alkane reacted, have been measured in the laboratory for C_7–C_{25} alkanes with linear, branched, and cyclic structures (Lim and Ziemann, 2005, 2009b; Presto et al., 2010; Tkacik et al., 2012). In these studies, SOA yields are reported after 50–85 % of the alkane had reacted and may not represent the maximum possible yield. Generally, SOA yield was found to increase with increasing carbon number or the presence of a cyclic structure and decrease with branching of the carbon chain.

SOA formation under low-NO_x conditions has received less attention. Yee et al. (2012, 2013) developed an oxidation mechanism for *n*-dodecane and extended it to cyclic and branched compounds. Yee et al. (2012, 2013) also identified multiple generations of alkane oxidation products, and Craven et al. (2012) used positive matrix factorization to demonstrate continuous evolution of the chemical composition of SOA generated during 36 h of low-NO_x dodecane photooxidation. SOA yields for select linear and cyclic structures have been measured, and the same trends for carbon number and presence of a cyclic structure were observed under low-NO_x conditions as under high-NO_x conditions (Lambe et al., 2012).

Here we report SOA yields from 12-carbon alkanes with linear, cyclic, and branched structures under both high- and low-NO_x conditions. In each experiment, 95–100 % of the alkane, a greater percentage than those achieved in previous chamber studies, was oxidized to study the contribution of multi-generation products to SOA yield. Additionally, multiple alkane concentrations were used to assess the effect of precursor concentration on gas-particle partitioning.

2 Materials and methods

2.1 Experimental setup

Low-NO_x experiments were conducted in the Caltech dual 28 m^3 Teflon chambers, details of which are given elsewhere (Cocker et al., 2001; Keywood et al., 2004). High-NO_x experiments were conducted in the Caltech dual 24 m^3 Teflon chambers, located in a new facility that replaced the 28 m^3 chamber facility. Most components of the old facility, including instrumentation, were moved to the new laboratory, which provides precise temperature control of the chambers (±1 °C) and flushing at a rate approximately 3 times faster than that in the 28 m^3 chamber facility. The difference in chamber volume is not expected to influence the experiment outcomes. Before each experiment, the chambers were flushed with dried, purified air for > 24 h, until the particle number concentration < 50 cm^{-3} and the volume concentration < 0.1 $\mu m^3\,cm^{-3}$. First, hydrogen peroxide (H_2O_2, 50 % wt., Sigma Aldrich) was added to the chamber by flowing purified air over a measured volume of H_2O_2 in a glass bulb maintained at 30–35 °C. Volumes of 70 and 280 µL were used for high-NO_x and low-NO_x, experiments, respectively. Next, seed particles were injected by atomizing a 0.015 M aqueous ammonium sulfate solution. *n*-Dodecane (Sigma Aldrich, 99+ % purity), 2-methylundecane (TCI, America, > 98 % purity), or hexylcyclohexane (TCI, America, > 98 % purity) was introduced into the chamber by evaporating a known alkane liquid volume with 5 $L\,min^{-1}$ of purified air. Cyclododecane (TCI, America, > 99 % purity) was introduced into the chamber by evaporating a known cyclododecane mass with 5 $L\,min^{-1}$ of purified air. During each injection, the glass bulb containing the liquid or solid alkane was heated slightly to facilitate evaporation. For high-NO_x experiments, approximately 100 ppbv NO was then added to the chamber from a 510 ppmv NO in N_2 cylinder (Air Liquide). The chamber contents were allowed to mix for 1 h before beginning irradiation with 350 nm-centered UV broadband lamps (40 W Sylvania 350BL). Different light intensities were used for low- and high-NO_x experiments corresponding to $j_{NO_2} \sim 4\times10^{-3}\,s^{-1}$ and $\sim 6\times10^{-3}\,s^{-1}$, respectively. To maintain high-NO_x conditions, 20 sccm of 510 ppmv NO was continuously injected into the chamber during the irradiation period. This additional ~ 21 L of N_2 has a negligible effect on chamber volume. The chamber contents were irradiated for 18 h and 30–36 h for high- and low-NO_x experiments, respectively, to achieve similar OH exposures in all experiments.

A suite of instruments was used to study the evolution of the gas and particle phases. Alkane concentrations were measured using a gas chromatograph with flame ionization detector (GC/FID, Agilent 6890N), equipped with a HP-5 column (15 m × 0.53 mm ID × 1.5 µm thickness, Agilent). Samples for injection into the GC/FID were taken by drawing 1.3 L of chamber air at a flow rate of 0.13 L min^{-3} through a glass tube packed with Tenax TA resin. The glass tube was subsequently desorbed for 10 min in the inlet of the GC/FID at 260 and 275 °C for low- and high-NO_x experiments, respectively, onto the column, held at 30 °C. After 15 min, the oven temperature was ramped at 10 °C min^{-1} to 280 °C and held at that temperature for 5 min. The mass response of the detector was calibrated for each alkane using Tenax tubes spiked with standard solutions and analyzed using the same method as the sample tubes. Relative humidity (RH), temperature, NO, NO_x, and O_3 were continuously monitored. Alkane oxidation products were detected using a custom-modified Varian 1200 triple-quadrupole chemical ionization mass spectrometer (CIMS). Details of operation can be found elsewhere (Crounse et al., 2006; Paulot et al., 2009; Yee et al., 2012, 2013). The CIMS was operated in negative mode in which CF_3O^- is used as the reagent ion. CF_3O^- clusters with the analyte, R, forming ions $[R \cdot CF_3O]^-$ at mass-to-charge ratio (m/z) $[M+85]^-$, where M is the nominal weight of R. For acidic species, the transfer product forms ions $[R \cdot F]^-$ at m/z $[M+19]^-$. Some analytes can be seen in both the cluster and transfer product forms. The signal at each m/z represents the sum of signals from all isomers contributing to that m/z.

Aerosol size distribution and number concentration were measured continuously using a custom-built scanning mobility particle sizer consisting of a differential mobility analyzer (DMA, TSI, 3081) coupled to a condensation particle counter (CPC, TSI, 3760), henceforth referred to as the DMA. The DMA was operated in a closed-loop

configuration with a recirculating sheath and excess flow of 2.67 L min^{-1} and a 5.4 : 1 ratio of sheath to aerosol flow rates. The column voltage was scanned either from 10 to 1000 V over 100 s or 15 to 9850 V over 45 s.

Real-time particle mass spectra were collected continuously by an Aerodyne high resolution time-of-flight aerosol mass spectrometer (AMS, DeCarlo et al., 2006; Canagaratna et al., 2007). The AMS switched between the higher resolution, lower sensitivity "W-mode" and the lower resolution, higher sensitivity "V-mode". AMS data were processed using the ToF-AMS Unit Resolution Analysis Toolkit, "SQUIRREL" (http://cires.colorado.edu/jimenez-group/ToFAMSResources/ToFSoftware/index.html), in Igor Pro Version 6.31 (Wavemetrics, Lake Oswego, OR). "V-mode" data were analyzed using a fragmentation table to separate sulfate, ammonium, and organic spectra and to time-trace specific mass-to-charge ratios (Allan et al., 2004). "V-mode" and "W-mode" data were analyzed using the high-resolution spectra toolbox known as PIKA (Peak Integration by Key Analysis) to determine the chemical formulas contributing to distinct m/z ratios (DeCarlo et al., 2006). Organic ions up to m/z 305 were used to calculate elemental ratios. Craven et al. (2012) proposed formulas for organic ions with $m/z > 100$ observed for low-NO_x dodecane photooxidation SOA based on hypothesized fragmentation of products formed in the dodecane photooxidation mechanism (Yee et al., 2012). Similar analysis was applied to identify organic ions with $m/z > 100$ for SOA from all 4 alkanes investigated here under both low- and high-NO_x conditions. Organic ions CO^+ and $C_2H_4^+$ were not fit in "V-mode" due to the large interference from the N_2^+ peak, and their signals were estimated from those of particle-phase CO_2^+ and $C_2H_3^+$, respectively, using correlations determined from "W-mode" data, which has better resolution of the CO^+, N_2^+, and $C_2H_4^+$ peaks. The ratio of particle-phase CO^+ to CO_2^+ varied by experiment between 0.45 and 3.5, and a specific ratio was used for each experiment (see Table S1). The ratio of $C_2H_4^+$ to $C_2H_3^+$ was found to be 0.47 for SOA from dodecane, 2-methylundecane, and hexylcyclohexane and 0.40 for SOA from cyclododecane under both NO_x conditions. Additionally, the intensities of H_2O^+, OH^+, and O^+ were calculated from particle-phase CO_2^+ (Aiken et al., 2008). AMS data reported in this work were collected using "V-mode" and averaged over 1 h or 30 min intervals for low- or high-NO_x experiments, respectively.

Experimental OH concentrations were calculated from the measured alkane concentration, the alkane concentration decay rate, estimated from the alkane concentration fit to a differentiable function (typically, a 1- or 2-term exponential function), and the alkane + OH reaction rate constant. A literature OH reaction rate constant was available only for dodecane; rate constants for the other three alkanes were estimated from a relative rate experiment in which 10 ppbv of each alkane was oxidized simultaneously under low-NO_x conditions (Table 1). The measured rate constant for hexylcyclohexane is in good agreement with that calculated from structure–activity relationships (Kwok and Atkinson, 1995), $17.6 \times 10^{-12}\,cm^3\,molec^{-1}\,s^{-1}$, and the measured rate constants for 2-methylundecane and cyclododecane are lower than those calculated from structure–activity relationships, 13.9×10^{-12} and $17.0 \times 10^{-12}\,cm^3\,molec^{-1}\,s^{-1}$, respectively. To calculate OH exposure, an interpolated OH concentration with a time resolution of 2–3 min is calculated from a fit to experimental data, as described previously, the alkane concentration decay rate, and the alkane + OH reaction rate constant. The interpolated OH concentration is multiplied by the time between data points and summed to each time point to obtain OH exposure.

Photolysis of H_2O_2 under low-NO_x conditions produced a constant OH radical concentration of $(1–3) \times 10^6$ molec cm^{-3}. Under high-NO_x conditions, OH radicals also were produced throughout the entire irradiation period, 18 h, with initial concentrations of $(0.7–3) \times 10^7$ molec cm^{-3} that decreased steadily to $(1–5) \times 10^6$ molec cm^{-3} after 18 h. In addition, reaction of HO_2 radicals with NO produced NO_2, which photolyzed to produce O_3. O_3 concentrations peaked at 200–600 ppbv approximately halfway through the experiment and then decreased as NO was continuously injected into the chamber. The variance in O_3 concentration is not expected to affect SOA formation mechanisms and is discussed below. Typical vapor concentrations and SOA growth for a high-NO_x experiment (59 ppbv dodecane) are shown in Fig. 1.

In addition to OH and O_3, NO_3 was produced under high-NO_x conditions. All oxidant concentrations varied over the course of the experiment due to the continuous addition of NO. While O_3 is not expected to react with most alkane photooxidation products, it can react with dihydrofurans, which also react with OH and NO_3. Jordan et al. (2008) estimated C_{12} dihydrofuran + OH rate constants as approximately $2.4 \times 10^{-13}\,cm^3\,molec^{-1}\,s^{-1}$. The rate constants for C_{12} dihydrofuran + O_3 and C_{12} dihydrofuran + NO_3 were taken as 3.49×10^{-15} and $1.68 \times 10^{-10}\,cm^3\,molec^{-1}\,s^{-1}$, respectively, as measured for 4,5-dihydro-2-methylfuran by Martin et al. (2002). Using measured O_3 concentrations and OH concentrations calculated from the alkane concentration decay, the lifetime of dihydrofuran against reaction with O_3 was calculated to be an order of magnitude less than the lifetime against reaction with OH for OH exposures $> 5 \times 10^6$ molec cm^{-3} h (elapsed time > 2 h). At lower OH exposures, reaction of dihydrofurans with OH were expected to dominate over that with O_3. NO_3 concentration was not measured directly, and model estimations varied by 3 orders of magnitude as O_3, NO_x, and OH concentrations varied during a modeled experiment. For the highest estimated NO_3 concentrations (1×10^7 molec cm^{-3}), the lifetime of dihydrofuran against reaction with NO_3 was comparable to that of reaction with O_3, and at the lowest estimated concentrations, the lifetime was an order of magnitude larger than that of reaction with OH. In an urban area such as Mexico City with peak OH, O_3, and NO_3 (daytime) concentrations of 4.6×10^6, $(0.74–2.0) \times 10^{12}$, and 2.4×10^7 molec cm^{-3}, respectively (Molina et al., 2010; Stephens et al., 2008; Volkamer et al., 2010), the estimated lifetimes of dihydrofuran against reaction with these compounds are 15 min, 2.4–6.4 min, and 4.1 min, respectively. The conditions in the present experiments are consistent with the shorter lifetime of dihydrofuran reaction against O_3 than OH in the atmosphere and, at the largest estimated NO_3 concentration, consistent with similar lifetimes of dihydrofuran reaction against O_3 and NO_3 in the atmosphere. Additionally, NO_3 is not a significant sink of either the parent alkane or RO_2 radicals even at the largest estimated NO_3 concentrations.

2.2 SOA yield calculations

Particles deposited to the chamber walls are accounted for when calculating the mass concentration of organic aerosol formed. Particle wall loss corrections were made using the two limiting assumptions of gas-particle partitioning (Weitkamp et al., 2007; Hildebrandt et al., 2009; Loza et al., 2012). In one limit, no suspended vapors are assumed to condense on deposited particles. This limit is termed the lower limit because it represents the smallest possible SOA mass formed during growth. In the other limit, deposited particles are assumed to interact with suspended vapors to the same extent as suspended particles. This limit is termed the upper limit because it represents the largest possible SOA mass formed during growth. A new approach to calculate both upper and lower limit wall loss solely from suspended particle number-size distribution data is described in Appendix A. This approach is an extension of the Aerosol Parameterization Estimation model (Pierce et al., 2008) to calculate both limits to particle wall loss corrections. Total particle volume concentration was calculated from the wall-loss corrected number-size distributions. To obtain SOA mass concentration, the seed particle volume concentration was subtracted from the total particle volume concentration, and the resulting organic particle volume concentration was multiplied by the SOA density, calculated from DMA and AMS data from a separate experiment (see Table 1).

SOA yield, Y, was calculated for both upper and lower limit SOA mass concentrations, ΔM_o ($\mu g\,m^{-3}$), using

$$Y = \frac{\Delta M_o}{\Delta HC} \tag{1}$$

where ΔHC ($\mu g\,m^{-3}$) is the mass concentration of alkane reacted.

In addition to particle-phase wall losses, vapor-phase wall losses of 12-carbon alcohols and ketones have been observed in laboratory chambers (Matsunaga and Ziemann, 2010). If vapors condense on chamber walls instead of on particles, then SOA yields will be underestimated. Vapor wall losses were not taken into account for the

yields presented here; the effect of vapor wall losses on SOA yields is discussed in Sect. 3.4.

3 Results and discussion

For most SOA precursors, a larger initial hydrocarbon concentration translates into a larger source of semivolatile oxidation products, assuming that reactions occur at the same temperature and oxidizing conditions and that the vapor-phase product distributions do not vary over the range of initial hydrocarbon concentrations considered. The presence of more condensible products facilitates partitioning of semivolatile product species to the particle phase, leading to increased yields relative to lower concentration experiments. Oxidant exposure also affects SOA yield. SOA yield increases with increasing oxidant exposure as the hydrocarbon reacts forming multiple generations of semivolatile products; however, with ever-increasing oxidation, fragmentation reactions will begin to dominate over functionalization reactions, producing volatile products that do not condense or evaporate from the condensed phase and decreasing SOA yield.

3.1 High-NO_x SOA yield measurements

Conditions for high-NO_x experiments are given in Table 2. The reported ΔM_o and yield correspond to approximately 18 h of irradiation and an OH exposure of (6–12) $\times 10^7$ molec cm^{-3} h. By this point, at least 95 % of the initial hydrocarbon had reacted. SOA growth occurred continuously as the alkane reacted. Figure 2a shows the SOA yield after approximately 18 h of irradiation as a function of hydrocarbon concentration reacted. The top and bottom of each line correspond to the upper and lower limits to the particle wall loss correction, respectively. Experiments were run with approximately 10 ppbv (100 $\mu g\,m^{-3}$) or 60–80 ppbv (400–550 $\mu g\,m^{-3}$) initial alkane concentration. In both initial alkane concentration regimes, cyclododecane produced the largest yields, while the smallest yields were observed for 2-methylundecane. Dodecane and hexylcyclohexane yields were similar. These results are consistent with the relationship between alkane structure and SOA yield observed by Lim and Ziemann (2009b) and Tkacik et al. (2012). When comparing the yields for each compound between the two initial hydrocarbon concentration regimes, no clear patterns emerge. For 2-methylundecane and hexylcyclohexane, the yield increases as initial alkane concentration increases. For dodecane and cyclododecane, the yield decreases as initial alkane concentration increases. This behavior will be discussed further in Sect. 3.5.

For cyclododecane and hexylcyclohexane, a large difference between upper and lower limit yields is observed in Fig. 2 for experiments with $\Delta HC < 100\,\mu g\,m^{-3}$. These experiments had approximately 10 ppbv initial alkane. For experiments shown in Fig. 2 with $\Delta HC > 100\,\mu g\,m^{-3}$, those with 60–80 ppbv initial alkane, SOA growth began soon after the onset of irradiation, increasing the suspended particle number-size distribution peak diameter to 250–350 nm. During the experiments with ~ 10 ppbv initial alkane, SOA growth did not begin immediately, and the suspended particle number-size distribution peak diameter remained below 200 nm for most of the experiment. The temporal trend of suspended particle number-size distribution peak diameter for the high-NO_x cyclododecane experiments is shown in Fig. S1. In the Caltech chambers, particle wall loss rate constants are lowest for 200–300 nm particles (Fig. S1, right panel). Typical seed particle number-size distribution peak diameters are 40–60 nm. Because particle growth is slower in ~ 10 ppbv initial alkane experiments and particles remain at a smaller diameter for longer times, more particles are lost to the wall before and during SOA growth in ~ 10 ppbv initial alkane experiments than in those with 60–80 ppbv initial alkane, owing to the size-dependence of particle wall loss. Therefore, a large difference between lower and upper limit yields is observed for the ~ 10 ppbv initial alkane experiments. Less overall SOA growth is observed for dodecane and 2-methylundecane; as a result, less difference is observed between the lower and upper limit yields.

SOA yields from cyclododecane were close to or greater than 1 depending on the wall loss correction method used. SOA yields can be > 1 if most of the functionalized oxidation products generated from a non-functionalized parent hydrocarbon condense

to form SOA. SOA yields > 1 have been observed previously from longifolene photooxidation under high-NO_x conditions (Ng et al., 2007a). To determine if the SOA mass produced violated mass conservation, an estimation of maximum potential SOA mass concentration was calculated assuming that all oxidation products formed from the reacted cyclododecane condensed. For the estimation, the average SOA molecular weight was calculated from the oxygen-to-carbon (O : C), hydrogen-to-carbon (H : C), and nitrogen-to-carbon (N : C) ratios measured by the AMS, assuming that condensed species retain 12 carbon atoms. Note that ions NO^+ and NO_2^+ are included in these calculations and will be discussed further in Sect. 3.5. To calculate the maximum potential SOA mass concentration, the molar concentration of cyclododecane reacted is multiplied by the average SOA molecular weight. This SOA mass concentration is then compared to the observed SOA mass concentration. For experiment CH1 (cyclododecane), the maximum potential SOA formed was $84\,\mu g\,m^{-3}$, which is greater than the lower wall loss limit ΔM_o but less than the upper wall loss limit ΔM_o. For experiment CH2 (cyclododecane), the maximum potential SOA formed was $519\,\mu g\,m^{-3}$, which is greater than both the lower and upper bound limit ΔM_o. All observed cyclododecane yields except for the upper wall loss limit yield for CH1 do not violate mass conservation. It is likely that uncertainties in deposited particle growth rates calculated in the upper limit wall loss correction method (see Appendix A) cause the upper limit yield for CH1 to be overestimated.

Previous studies exist of SOA yields under high-NO_x conditions for dodecane, 2-methylundecane, and cyclododecane. Lim and Ziemann (2009b) measured SOA yields for all three compounds with initial alkane concentrations of approximately 1 ppmv, of which 76–83 % was oxidized at the point at which yields were calculated. In the present work, yields were calculated for lower initial alkane concentrations with a larger fraction of the initial alkane reacted. Because higher initial alkane concentration and lower extent of alkane reacted have opposite effects on SOA yield that are difficult to decouple, comparison of absolute measurements between Lim and Ziemann (2009b) and the present work are not instructive. Presto et al. (2010) reported SOA yields for dodecane oxidation for 19.1 and 57.8 ppbv initial alkane, and Tkacik et al. (2012) reported SOA yields from 2-methylundecane oxidation for a low alkane concentration (initial alkane concentrations were not specified). Both studies parameterized yields using the volatility basis set (VBS) for $\Delta M_o < 50\,\mu g\,m^{-3}$. A comparison of the present work to these studies is shown in Fig. 3. Both Presto et al. (2010) and Tkacik et al. (2012) report the upper limit to particle wall losses. For comparison to these previous studies, the upper limit to particle wall losses and a unit SOA density were used to calculate yields for experiments DH1, DH2, DH3, MH1, and MH2 shown in Fig. 3. The dodecane VBS parameterization presented by Presto et al. (2010) matches the higher final ΔM_o dodecane experiments, DH2 and DH3, for $\Delta M_o < 50\,\mu g\,m^{-3}$; however, it does not match the lower final ΔM_o dodecane experiment, DH1. This discrepancy can be attributed to different OH exposure. Presto et al. (2010) achieved an OH exposure of approximately 1.2×10^7 molec cm^{-3} h and did not react all of the parent alkane, whereas OH exposure in the present experiments was approximately 7×10^7 molec cm^{-3} h and at > 95 % of the parent alkane reacted. Similar results are observed when comparing 2-methylundecane yields from Tkacik et al. (2012) with those in the present study. The OH exposure achieved in Tkacik et al. (2012), 6×10^6 molec cm^{-3} h, was also lower than that achieved in the present work.

3.2 Low-NO_x SOA yield measurements

Conditions for low-NO_x experiments are presented in Table 3. ΔM_o and SOA yield measurements are reported after 30–36 h irradiation, corresponding to OH exposures of (6–12) $\times 10^7$ molec cm^{-3} h, for which at least 95 % of the initial alkane reacted. Figure 2b shows the SOA yield after 30–36 h irradiation, and, as for the high-NO_x data, the top and bottom of each line correspond to the upper and lower limits to the particle wall loss correction, respectively. The highest yields are observed for cyclododecane, followed by hexylcyclohexane, with the yields for dodecane and 2-methylundecane being similar. The ordering of hexylcyclohexane, dodecane, and 2-methylundecane yields is different from that observed under high-NO_x conditions and will be discussed further in

Sect. 3.5. As with the high-NO_x yields, there are no compound-specific trends for SOA yield with initial alkane concentration.

SOA yields under low-NO_x conditions have not been reported previously for the compounds studied here. SOA yields under low-NO_x conditions have been reported for *n*-decane and *n*-pentadecane in a Potential Aerosol Mass flow reactor (Lambe et al., 2012). Lambe et al. (2012) reported maximum yields of 0.39 and 0.69 at OH exposures of 1.4×10^8 and 9.7×10^7 molec cm^{-3} h and SOA concentrations of 231 and 100 $\mu g\,m^{-3}$ for decane and pentadecane, respectively. The dodecane SOA yield is expected to lie between those for longer and shorter chain alkanes; however, the dodecane SOA yields measured in the present study (Table 3) are less than that measured for 231 $\mu g\,m^{-3}$ decane, a much larger initial concentration than those used in the present experiments, by Lambe et al. (2012) at similar OH exposure. Lambe et al. (2012) note that the maximum SOA yield for pentadecane at 16 $\mu g\,m^{-3}$ is 0.21, which is in much better agreement with the dodecane SOA concentrations and SOA yields in the present study.

3.3 Comparison of SOA yields under high- and low-NO_x conditions

High- and low-NO_x SOA yields for each of the alkanes as a function of cumulative OH exposure using lower and upper limits to particle wall loss corrections are shown in Figs. 4 and 5, respectively. The same trends are observed for each limiting case. For a number of SOA systems, SOA yields are higher under low-NO_x conditions than under high-NO_x conditions (e.g. Song et al., 2005; Ng et al., 2007a; Eddingsaas et al., 2012). A likely explanation is that alkoxy radicals (RO) produced from the reaction of alkyl peroxy radicals (RO_2) and NO undergo fragmentation to form higher volatility species, whereas hydroperoxides produced from the reaction of RO_2 and HO_2 do not. With less fragmentation under low-NO_x conditions, the carbon chain is preserved, resulting in higher yields when compared with those observed for high-NO_x conditions. For linear alkanes with > 6 carbons, isomerization of RO is favored over fragmentation reactions or reaction with O_2, preserving the carbon chain and producing compounds of lower volatility than fragmentation products (Lim and Ziemann, 2009a). As a result, yields under low- and high-NO_x conditions for these larger alkanes are similar. The effects of parent alkane structure and NO_x conditions will be discussed further in Sect. 3.6.

Maximum SOA yields are achieved after (4–6) $\times 10^7$ molec cm^{-3} h OH exposure regardless of NO_x condition. Lambe et al. (2012) observed an increase, peak, and decrease of SOA yield with increasing OH exposure attributable to a transition from functionalization to fragmentation reactions; the OH exposures achieved in the present study were not large enough to observe similar phenomena.

In Fig. 3, it is interesting to note that different SOA yields are observed from the same alkane and ΔM_o for different initial alkane concentrations (e.g. at $\Delta M_o = 10\,\mu g\,m^{-3}$, the yield from 9 ppbv dodecane, DH1, is 0.27, whereas the yield from 57–61 ppbv dodecane, DH2 and DH3, is 0.06). This trend is observed for all four compounds under both high- and low-NO_x conditions and suggests that parameterizing yields for these alkanes in terms of ΔM_o, i.e. assuming quasi-equilibrium growth, is not useful.

Shiraiwa et al. (2013) predicted that the behavior of the particle size distribution during low-NO_x dodecane photooxidation is consistent with kinetically limited, rather than quasi-equilibrium, growth. Other ambient and laboratory studies also suggest that SOA growth can be kinetically limited (Riipinen et al., 2011; Perraud et al., 2012). For kinetically limited SOA growth, SOA yield should be a function of total particle surface area; however, for the same alkane and NO_x conditions and a given particle surface area, different SOA yields were observed, similar to the results presented in Fig. 3. Instead, SOA yields were parameterized by number of semivolatile organic compound (SVOC)-particle collisions. Total SVOC concentration was simulated for the case of dodecane low-NO_x photooxidation using a kinetic multi-layer model of gas-particle interactions (KM-GAP) (Shiraiwa et al., 2012; Shiraiwa and Seinfeld, 2012; Shiraiwa et al., 2013). KM-GAP explicitly resolves mass transport and chemical reactions in the gas and particle phases. In the model, the collision flux of SVOC at the particle surface, J_A

(molec cm^{-3} s^{-1}), is

$$J_A = \frac{1}{4} c_A \bar{c}_A \quad (2)$$

where c_A is the SVOC concentration (molec cm^{-3}) and $\bar{c}_A$ is the mean molecular speed of SVOC (cm s^{-1}). J_A can be calculated for discrete time points, i, in an experiment corresponding to particle surface area measurements. The following summation is used to calculate cumulative number of SVOC-particle collisions per unit chamber volume, C_{sum} (cm^{-3}),

$$C_{sum} = \sum_{i=1}^{n} J_{A,i} S_i \Delta t_i \quad (3)$$

where n is the total number of data points, S_i is the particle surface area (cm^2 cm^{-3}), and Δt_i is the time between data points i and $i+1$ (s). Here the upper limit wall-loss corrected surface area concentration is used to correspond to the model, which does not simulate particle wall losses. Figure 6 shows yield as a function of C_{sum} for the dodecane low-NO_x photooxidation system. Calculations were made with a time resolution of 3 min, but hourly averaged data are displayed. The SOA yields from both experiments trend similarly with C_{sum}. This result indicates that analysis of chamber experiments with kinetic-flux modeling is instructive and that parameterizing SOA yields simply as a function of ΔM_o may not always be suitable.

3.4 Effect of vapor wall losses on SOA yields

Condensible species can partition to suspended particles, deposited particles, and the chamber walls. The SOA yields reported here account for the first two processes, but vapor wall losses are not considered. If vapors are lost to the wall instead of forming SOA, then SOA yield will be underestimated. Matsunaga and Ziemann (2010) observed vapor wall losses for alkanes, ketones, and alcohols that are relevant to compounds formed in the present systems. The extent of vapor phase wall losses in both of the Caltech chamber facilities was investigated using experiments in which a known volume of dodecanone, dodecanol, or dodecane was injected into a chamber filled with purified air. The signal for each species was monitored over a period of several hours. Dodecane wall losses were not significant in either chamber. In the 28 m^3 chamber used for low-NO_x experiments, 2-dodecanone wall losses followed first-order kinetics with a rate constant of $k_w = 2.2 \times 10^{-6}\,s^{-1}$ ($\tau = 5.3$ days). In the 24 m^3 chamber used for high-NO_x experiments, 2-dodecanol wall losses followed first-order kinetics with a rate constant of $k_w = 1.5 \times 10^{-6}\,s^{-1}$ ($\tau = 7.7$ days). Matsunaga and Ziemann (2010) observed 20 % wall loss of 2-dodecanol in 80 min and 25 % wall loss of 2-dodecanone in 25 min, which equate to first order wall loss rate constants of $k_w = 3.4 \times 10^{-4}\,s^{-1}$ ($\tau = 49$ min) and $k_w = 9.2 \times 10^{-4}\,s^{-1}$ ($\tau = 18$ min) for 2-dodecanol and 2-dodecanone, respectively; after the initial decrease, the 2-dodecanone concentration remained constant for 400 min, presumably after equilibrium was achieved between the suspended vapors and those sorbed to the walls. Equilibrium was not observed for either compound in the Caltech chambers over a 22 h period, and it was not possible to detect rapid initial losses in the Caltech chambers as a result of the chamber setup and injection procedures. The time required to inject measurable concentrations of each compound into the chamber was at least 25 min, and because there is no active mixing in the Caltech chambers, it was necessary to wait an additional 20 min after the end of the injection for the chamber contents to mix. Rapid vapor wall losses occurring during this time period are difficult to distinguish from changes in compound concentration due to injection and mixing. Finally, alkane photooxidation generates a variety of products with multiple functionalization; however, only singly-functionalized compounds were tested for wall loss. Matsunaga and Ziemann (2010) showed that vapor wall loss is a function of compound vapor pressure and structure; therefore, it is difficult to extrapolate wall loss rates of 2-dodecanol and 2-dodecanone to all compounds formed from alkane photooxidation. In an attempt to quantify vapor wall losses, Shiraiwa et al. (2013) as-

sumed vapor wall losses follow pseudo-first order kinetics and varied vapor wall loss rate constants of SVOCs generated in KM-GAP simulations of dodecane low-NO_x photooxidation. Using $k_w = 9.6 \times 10^{-6}\,s^{-1}$, the highest value considered, led to a decrease of the SOA mass concentration by approximately 30 %. As a result, SOA yield would increase by 30 %. The combined uncertainties of vapor and particle phase wall loss result in a factor of 2–3 difference between the upper and lower limits to SOA yields in each system.

3.5 Aerosol chemical composition

Organonitrates have been identified previously as products from alkane high-NO_x photooxidation and are expected to be present in the particle phase (Lim and Ziemann, 2005). The AMS can detect organic nitrates as NO^+ and NO_2^+, but inorganic nitrates also contribute signal to these ions (Farmer et al., 2010). During the high-NO_x experiments, NO^+ and NO_2^+ trend with organic growth measured by the AMS. During this time, nitric acid is also formed from reaction of NO_2 with OH and can partition to particles and interact with the ammonium sulfate seed. The ratio of $NO^+ : NO_2^+$ observed during photooxidation experiments is higher than that from AMS ionization efficiency calibrations, in which ammonium nitrate is atomized into the AMS, indicating that the NO^+ and NO_2^+ signals are unlikely from inorganic nitrates. Because there is evidence that the signals for NO^+ and NO_2^+ likely come from organonitrates in the present experiments, these ions are included when calculating the total organic mass from AMS data. According to a proposed decomposition pathway for organonitrates (Francisco and Krylowski, 2005; Farmer et al., 2010), the oxygens in NO^+ and NO_2^+ are not bound directly to a carbon atom. Therefore, the ion signals at NO^+ and NO_2^+ were not included in elemental ratios used to calculate average carbon oxidation state.

Average carbon oxidation state, $\overline{OS}_C$, (Kroll et al., 2011) was calculated from AMS measurements for comparison of the alkane systems. SOA $\overline{OS}_C$ from each parent alkane showed similar trends with respect to initial alkane concentration, NO_x conditions, and OH exposure; therefore, data only for cyclododecane are shown in Fig. 7. Under both high- and low-NO_x conditions, SOA formed from a lower initial cyclododecane concentration was characterized by a higher $\overline{OS}_C$. This trend has been observed in other systems (Shilling et al., 2009) and is expected because a higher initial alkane concentration increases the concentrations of semivolatile products, which have lower $\overline{OS}_C$ than low volatility products, in both the gas and particle phases. Under low-NO_x conditions, SOA $\overline{OS}_C$ decreases for OH exposures of 0–2 × 10^7 molec cm^{-3} h and then gradually increases with increasing OH exposure. Other studies have reported similar trends for O : C formed under low-NO_x conditions (Lambe et al., 2012; Loza et al., 2012). This trend is attributed to initial condensation of a small amount of low-volatility oxidation products followed by condensation of semivolatile products as the SOA mass increases, and then condensation of more low-volatility products as gas-phase oxidation progresses. Under low-NO_x conditions, over 95 % of the aerosol mass measured by the AMS in the present experiments comes from ions with chemical formulae of $C_xH_y^+$, $C_xH_yO^+$, and $C_xH_yO_2^+$. Initially, the contributions of ions with formula $C_xH_y^+$ are approximately equal to the sum of those with formulae $C_xH_yO^+$ and $C_xH_yO_2^+$, but as OH exposure increases to 2 × 10^7 molec cm^{-3} h, the contributions from ions with formula $C_xH_y^+$ begin to dominate, presumably as more semivolatile species condense. At OH exposures above 2 × 10^7 molec cm^{-3} h, contributions from ions with formulae $C_xH_yO^+$ and $C_xH_yO_2^+$ increase and those with formula $C_xH_y^+$ decrease but still comprise a majority of the organic mass. For low-NO_x alkane photooxidation, it has been suggested that peroxyhemiacetal formation triggers initial SOA growth (Yee et al., 2012, 2013; Shiraiwa et al., 2013). The hydroperoxides thought to contribute to initial peroxyhemiacetal formation, such as the carbonyl hydroperoxide, have multiple functional groups, which could explain the initial, higher $\overline{OS}_C$ values. As the particles grow, other, less functionalized oxidation products can also condense, decreasing $\overline{OS}_C$. As oxidation continued, multiple generations of gas-phase oxidation products, such as hydroxy carbonyl hydroperoxides and dicarbonyl hydroperoxides, were observed in dodecane

photoxidation and proposed for cyclododecane photoxidation and also could partition to particles, increasing $\overline{OS}_C$. Although the proposed SOA products have multiple oxygen moities, much of the carbon chain is not functionalized, and $C_xH_y^+$ fragments are expected to dominate the mass spectrum.

Under high-NO_x conditions, an initial decrease in $\overline{OS}_C$ was not prominent, and the increase in $\overline{OS}_C$ as OH exposure increased was less when compared to that under low-NO_x conditions. When comparing high- and low-NO_x experiments with similar initial cyclododecane concentration (CL2 with CH1 or CL3 with CH2), SOA formed under high-NO_x conditions has a higher $\overline{OS}_C$ during SOA growth but similar $\overline{OS}_C$ after all cyclododecane reacted. These trends indicate that less OH exposure is required to form low-volatility products under high-NO_x conditions than under low-NO_x conditions. A similar trend was observed by Presto et al. (2009), who used a thermodenuder to measure the volatility of heptadecane SOA formed under high- and low-NO_x conditions. The estimated vapor pressures of many of the condensible species produced under high- and low-NO_x dodecane photooxidation are similar (Jordan et al., 2008; Yee et al., 2012), but the experimental conditions control the rate at which these compounds are formed.

Alkane oxidation by OH generates RO_2, which can react with NO, HO_2, or another RO_2. RO_2 can also react with NO_2, but the peroxynitrates formed quickly decompose back to RO_2 and NO_2; this pathway will not be considered here. In the present experiments, RO_2 reacted primarily with HO_2 under low-NO_x conditions and with NO under high-NO_x conditions. NO concentration was measured directly and varied from 2–100 ppbv, and HO_2 concentration was estimated from a photochemical model as approximately 1 × 10^{10} cm^{-3} (Yee et al., 2012). Using RO_2 reaction rate constants from the Master Chemical Mechanism 3.2 (http://mcm.leeds.ac.uk/MCM; Jenkin et al., 2003; Saunders et al., 2003), the lifetimes of RO_2 reaction with NO and HO_2 are estimated as 0.04–2 and 4 s, respectively. Shorter RO_2 lifetimes under high-NO_x conditions will allow low-volatility products to form at lower OH exposures.

3.6 Effect of gas-phase fragmentation reactions on SOA yield

Additional trends between alkane structure, bulk SOA chemical composition, and SOA yield can be observed from the AMS mass spectra. Ions can be grouped into "families" according to their elemental composition. The mass spectra are dominated by ions in family CH, ions with formula $C_xH_y^+$, and family CHO1, ions with formula $C_xH_yO^+$. Figures 8 and 9 show the contribution of ions in each family as a function of the number of carbon atoms in each ion and the total family contribution for a 30 min averaged sample obtained after 95–100 % of the initial alkane concentration reacted. Only data from experiments with higher alkane concentration (> 50 ppbv and > 25 ppbv for high- and low-NO_x, respectively) are shown; similar trends were observed in experiments with lower initial alkane concentrations. In the present study, an increase in yield is characterized by larger mass fractions of ions containing 9 or more carbon atoms. Under high-NO_x conditions, the total mass fractions of family CH ions for cyclododecane and dodecane SOA are higher than those for 2-methylundecane and hexylcylohexane SOA (Fig. 8a), and the trend is reversed for ions in family CHO1 (Fig. 8). The same trend is not observed under low-NO_x conditions, although compounds with a larger mass fraction of family CH ions have smaller mass fractions of family CHO1 ions. These trends provide insight into the significance of gas-phase fragmentation reactions under high- and low-NO_x conditions.

During photooxidation, the prevalence of branching in a compound is expected to lead to increased fragmentation, requiring more functionalization to produce condensible species. Greater functionalization increases the oxygen content of product molecules, thus it is reasonable that SOA from branched compounds, 2-methylundecane and hexylcyclohexane, has a higher mass fraction of family CHO1 ions than that from compounds with less branching, cyclododecane and dodecane. These trends are not as apparent under low-NO_x conditions, suggesting that the fragmentation pathway may not be as important under low-NO_x conditions as under high-NO_x conditions. It should be noted that while fragmentation occurs for cyclododecane

oxidation products, it results in ring-opening, which preserves the carbon backbone and does not produce a higher-volatility species. Hexylcyclohexane is also a cyclic compound, and an alkoxy radical on the ring α to the branch point may result in ring-opening, which preserves the carbon backbone; thus, fragmentation of hexylcyclohexane will not always result in generation of species with fewer carbon atoms than the parent molecule.

Gas-phase fragmentation products from high-NO_x alkane photooxidation were detected using the CIMS (Table S3). The proposed products have been grouped into "families" by functionality: carboxylic acid ($C_nH_{2n}O_2$), hydroxy carboxylic acid ($C_nH_{2n}O_3$), carbonyl nitrate ($C_nH_{(2n-1)}NO_4$), or hydroxynitrate ($C_nH_{(2n+1)}NO_4$), where n is the number of carbon atoms in the proposed molecule. Figure 10 shows the signal for each product, normalized by ΔHC for a 30 min averaged sample obtained after 95–100 % of the initial alkane concentration reacted. The data are presented assuming that CIMS sensitivity is independent of n for a given family and that sensitivity is the same for all isomers (including cyclic and branched structures) for a given n and family. Concentration calibrations were not performed for all species presented, and trends of ion signal with carbon number are not evaluated. Because the CIMS has unit mass resolution and can detect ions produced as transfer ($m/z = [M+19]^-$) and cluster ($m/z = [M+85]^-$) products, the signals in Fig. 10b could come from an acid or a hydroperoxide. Under high-NO_x conditions, hydroperoxide production is not expected. For almost all products shown in Fig. 10, signals in the cyclododecane experiment are lower than those for the other three alkanes, suggesting that cyclododecane oxidation products undergo little fragmentation, consistent with trends obtained from AMS data. More fragmentation of 2-methylundecane and hexylcyclohexane oxidation products is expected than for those of dodecane; however, the signal from fragmentation products for most families are similar for dodecane, 2-methylundecane, and hexylcyclohexane, suggesting that some fragmentation also occurs during dodecane high-NO_x photooxidation.

Gas-phase fragmentation reactions can also occur under low-NO_x conditions from hydroperoxide photolysis (Yee et al., 2012, 2013). Photolysis of a hydroperoxide forms an alkoxy radical, which can isomerize or decompose depending on the carbon backbone structure. For dodecane, hydroperoxide photolysis is expected to be a minor reaction pathway compared with OH oxidation. The specific case of photolysis of a hydroperoxy group adjacent to a carbonyl produces an aldehyde, which has been shown to react with hydroperoxides to form peroxyhemiacetals. Peroxyhemiacetal formation is proposed to initiate SOA growth in the alkane low-NO_x photooxidation system (Yee et al., 2012, 2013; Shiraiwa et al., 2013). In this case, fragmentation reactions depend more on the relative position of hydroperoxy and carbonyl groups than the structure of the carbon backbone.

When comparing SOA yields between low- and high-NO_x conditions for each compound (Fig. 4), three dominant trends are observed. (1) Under high-NO_x conditions, SOA yields for dodecane and cyclododecane are larger for lower initial alkane concentration. (2) For hexylcyclohexane and, more noticeably, 2-methylundecane, SOA yields under high-NO_x conditions are higher when the initial alkane concentration is higher. (3) SOA yields for dodecane and cyclododecane are higher under high-NO_x conditions than under low-NO_x conditions. Trends (1) and (2) arise from the role of fragmentation under high-NO_x conditions. At higher initial alkane concentrations, semivolatile species can condense preferentially to particles, whereas, for lower initial alkane concentrations, semivolatile species remain in the gas phase for further oxidation. For linear or cyclic compounds, further oxidation decreases compound volatility, resulting in additional SOA formation and higher SOA yields. However, for branched compounds, further oxidation results in fragmentation, leading to higher volatility species that do not condense to form additional SOA. At sufficiently high OH exposures, fragmentation will become important for all systems that form SOA (Lambe et al., 2012), but those conditions were not reached in the present experiments. Trend (3) results from differences in the extent of fragmentation under both NO_x conditions. Dodecane and 2-methylundecane have almost identical chemical structures, and one may expect these two compounds to have similar SOA yields. Under low-NO_x conditions, the SOA yields for experiments ML2 and DL2 are 15–31 % (however, the SOA yield observed in ML1

is higher than that observed in DL1), whereas under high-NO_x conditions, higher SOA yields are observed for dodecane than for 2-methylundecane (see Tables 2 and 3). High-NO_x SOA yields are greater than low-NO_x yields for unbranched compounds, but high- and low-NO_x SOA yields are similar for branched compounds as a result of enhanced fragmentation under high-NO_x conditions.

4 Conclusions

In the present study SOA yields have been measured for linear, cyclic, and branched 12-carbon alkanes under high- and low-NO_x conditions in which 95–100 % of the alkane reacted. The highest SOA yields were observed from cyclic alkanes, and the presence of branch points decreased SOA yield, primarily under high-NO_x conditions where vapor-phase fragmentation reactions were more likely to occur. Uncertanties arise in the SOA yield measurements due to particle and vapor wall losses and result in a factor of 2–3 difference between upper and lower limits to SOA yield. Recently, Gentner et al. (2012) assessed SOA formation from diesel and gasoline vehicles and noted that SOA yields for cyclic alkanes with five- and six-membered rings, which comprise 37 % of diesel and 11 % of gasoline, were not well-characterized. This study presents data for one such compound, hexylcyclohexane. Hexylcyclohexane SOA yield was similar to that of dodecane under high-NO_x conditions and greater than dodecane under low-NO_x conditions. Lim and Ziemann (2009b) measured SOA yields for two other branched-cyclic compounds, *n*-butylcyclohexane and *n*-decylcyclohexane, under high-NO_x conditions but with initial alkane concentrations much higher than ambient concentrations, approximately 1 ppmv. The authors found that the SOA yield for butylcyclohexane was higher than that for decane, but the yield for decylcyclohexane was less than that for hexadecane. Further characterization of yields from branched-cyclic compounds is necessary to better identify trends and provide more data for models.

Although alkanes are emitted primarily in urban areas under high-NO_x oxidizing conditions, their relatively slow OH reaction rates allow for transport to rural areas with lower NO_x conditions. SOA yields measured in the present study are higher or the same under high-NO_x conditions in comparison to those measured for low-NO_x conditions. Therefore, alkanes exhibit the largest SOA formation potential in urban areas close to their sources.

Appendix A

Particle wall loss calculations

Pierce et al. (2008) developed the Aerosol Parameter Estimation model to determine the time variance of particle wall loss rates during an environmental chamber experiment. We have adapted this model to calculate the mass growth rate of suspended particles throughout an experiment. These mass growth rates are then applied to deposited particles to calculate lower and upper limit wall-loss corrections.

The model utilized in the current work is based on the aerosol General Dynamic Equation (Seinfeld and Pandis, 2006):

$$\frac{\partial n_s\left(D_p,t\right)}{\partial t} = \left(\frac{\partial n_s\left(D_p,t\right)}{\partial t}\right)_{\text{coag}} + \left(\frac{\partial n_s\left(D_p,t\right)}{\partial t}\right)_{\text{cond}} + \left(\frac{\partial n_s\left(D_p,t\right)}{\partial t}\right)_{\text{wl}} \tag{A1}$$

where $n_s\left(D_p,t\right)$ ($\text{cm}^{-3}\,\text{cm}^{-1}$) is the suspended particle number-size distribution, D_p (cm) is particle diameter, t (s) is time, and coag, cond, and wl represent the change in suspended particle size-number distribution due to coagulation, condensation, and particle-phase wall loss, respectively.

The change in the suspended particle number-size distribution due to coagulation is described by

$$\begin{aligned}\left(\frac{\partial n_s\left(D_p,t\right)}{\partial t}\right)_{\text{coag}} &= \frac{1}{2}\int_0^{D_p} K\left(\left(D_p^3-q^3\right)^{\frac{1}{3}},q\right) n_s\left(\left(D_p^3-q^3\right)^{\frac{1}{3}},t\right) n_s(q,t)\,\mathrm{d}q \\ &\quad - n_s\left(D_p,t\right)\int_0^{\infty} K\left(q,D_p\right) n_s(q,t)\,\mathrm{d}q\end{aligned} \tag{A2}$$

where $K\left(D_{p1},D_{p2}\right)$ ($\text{cm}^3\,\text{s}^{-1}$) is the coagulation coefficient for collisions of particles with diameters D_{p1} and D_{p2} (Seinfeld and Pandis, 2006). The DMA measures particle number-size distributions using discrete size bins, and the coagulation coefficient must also be discretized to be applied to these data. The change in suspended particle number-size distribution due to coagulation becomes

$$\begin{aligned}\left(\frac{\partial n_s\left(D_p,t\right)}{\partial t}\right)_{\text{coag}} &= \frac{1}{2}\sum_i\sum_j f_c\left(D_{pi},D_{pj}\right) K\left(D_{pi},D_{pj}\right) N\left(D_{pi},t\right) N\left(D_{pj},t\right) \\ &\quad - \sum_i K\left(D_{pi},D_{pk}\right) N\left(D_{pi},t\right) N\left(D_{pk},t\right)\end{aligned} \tag{A3}$$

where $f_c\left(D_{pi},D_{pj}\right)$ expresses whether the collision of a particle in size bin i with a particle in size bin j produces a particle in size bin k, bounded by diameters D_{pk-} and D_{pk+}:

$$f_c\left(D_{pi},D_{pj}\right) = 1 \quad \text{if} \qquad D_{pk-} \le 2\left(\left(\frac{D_{pi}}{2}\right)^3 + \left(\frac{D_{pj}}{2}\right)^3\right)^{\frac{1}{3}} < D_{pk+} \tag{A4}$$

$$f_c\left(D_{pi},D_{pj}\right) = 0 \quad \text{otherwise.} \tag{A5}$$

Particles are not allowed to form outside of the measured size range (Verheggen and Mozurkewich, 2006).

The change in suspended particle number-size distribution due to condensation is described by

$$\left(\frac{\partial n_s\left(D_p,t\right)}{\partial t}\right)_{\text{cond}} = -\frac{\partial}{\partial D_p}\left[I\left(D_p,t\right)n\left(D_p,t\right)\right] \tag{A6}$$

where $I\left(D_p,t\right)$ ($\mathrm{cm\,s^{-1}}$) is the rate of change of particle diameter as a result of condensation. Assuming spherical particles with a density ρ_p ($\mathrm{g\,cm^{-3}}$) that is not a strong function of time,

$$I\left(D_p,t\right) = \frac{\mathrm{d}D_p}{\mathrm{d}t} = \frac{2\sum J_i}{\pi D_p^2 \rho_p} \tag{A7}$$

where J_i ($\mathrm{g\,s^{-1}}$) is the mass flux of species i to the particle. J_i is defined as

$$J_i = \frac{2\pi D_p D_i M_i}{RT} f(Kn,\alpha_i)\left(p_{\infty,i} - p_{s,i}\right) \tag{A8}$$

where D_i ($\mathrm{cm^2\,s^{-1}}$) is the diffusion coefficient for species i in air, M_i ($\mathrm{g\,mol^{-1}}$) is the molecular weight of species i, R ($\mathrm{g\,cm^2\,s^{-2}\,mol^{-1}\,K^{-1}}$) is the gas constant, T (K) is temperature, $f(Kn,\alpha_i)$ is a correction factor for non-continuum effects and surface accommodation effects, $p_{\infty,i}$ ($\mathrm{g\,cm^{-1}\,s^{-2}}$) is the vapor pressure of species i in far from the particle, and $p_{s,i}$ ($\mathrm{g\,cm^{-1}\,s^{-2}}$) is the partial pressure of species i at the surface of the particle. Substituting Eqs. (A7) and (A8) into Eq. (A6) yields

$$\left(\frac{\partial n_s\left(D_p,t\right)}{\partial t}\right)_{\text{cond}} = \frac{-4}{RT\rho_p}\left[\sum_i D_i M_i f(Kn,\alpha_i)\left(p_{\infty,i} - p_{s,i}\right)\right]\frac{\partial}{\partial D_p}\left[\frac{1}{D_p}n_s\left(D_p,t\right)\right] \tag{A9}$$

Here we are assuming that ρ_p is constant with respect to D_p at a given time t. If many size bins are used to describe the particle number-size distribution, then ρ_p is likely constant over a small range of D_p, and the magnitude of the error that this assumption produces is reduced. Following Pierce et al. (2008), the unknown parameters in Eq. (A9) can be combined into a single factor, F_c ($\mathrm{cm^2\,s^{-1}}$), defined as

$$F_c = \frac{4}{RT\rho_p}\sum_i D_i M_i f(Kn,\alpha_i)\left(p_{\infty,i} - p_{s,i}\right) \tag{A10}$$

Substituting F_c into Eq. (A9) and differentiating gives the final form for the change in suspended number-size distribution due to condensation:

$$\left(\frac{\partial n_s\left(D_p,t\right)}{\partial t}\right)_{\text{cond}} = -F_c\left[-\frac{1}{D_p^2}n_s\left(D_p,t\right) + \frac{1}{D_p}\frac{\partial n_s\left(D_p,t\right)}{\partial D_p}\right] \tag{A11}$$

The model varies F_c to produce a number-size distribution that best fits the observed number distribution.

The change in suspend particle number-size distribution due to particle wall deposition is assumed to follow first-order kinetics with particle size-dependent rate constants, $\beta\left(D_p\right)$ ($\mathrm{s^{-1}}$):

$$\left(\frac{\partial n_s\left(D_p,t\right)}{\partial t}\right)_{\text{wl}} = -\beta\left(D_p\right)n_s\left(D_p,t\right) \tag{A12}$$

A theoretical determination of β is described in Crump and Seinfeld (1981) and McMurry and Rader (1985), however, parameters needed to calculate β values are difficult to quantify from theory alone for environmental chambers. Instead, β values can be determined from calibration experiments (Keywood et al., 2004; Ng et al., 2007b; Loza et al., 2012) or can be specified as unknowns in an aerosol general dynamic model (Pierce et al., 2008). The present model employs the former parameterization β

values. β values for AS particles are measured during calibration experiments in which wall deposition is the dominant process affecting the number distribution. Particles containing organics are assumed to behave the same as pure AS particles.

To implement the model, the General Dynamic Equation is solved numerically between each time step for a given experimental dataset. First the General Dynamic Equation is discretized into diameter size bins corresponding to those of the measured number-size distribution. Then the model is initialized with a measured number-size distribution at time step t and a guess for the parameter F_c. The model is solved using a Dormand Price pair 4th and 5th order Runge–Kutta method to produce a number-size distribution at time step $t+1$. The fit of the predicted to the observed number-size distributions at time step $t+1$ is quantified using various diameter moments. The ith diameter moment is calculated as follows

$$M_i = \int_0^\infty D_p^i n_s \left(D_p\right) \mathrm{d}D_p = \sum_k D_{p,k}^i N_s \left(D_{p,k}\right) \tag{A13}$$

where k is the size bin and N_s (cm^{-3}) is the suspended particle number concentration. The best fit of the predicted to the observed number distribution is that which minimizes χ^2:

$$\chi^2 = \sum_{a=1}^{9} \left(\frac{M_{i(a),p} - M_{i(a),o}}{M_{i(a),o}} \right)^2 \tag{A14}$$

where $i(a)$ is the set of diameter moments $[-1, -0.5, 0, 0.5, 1, 1.5, 2, 2.5, 3]$ and moment subscripts p and o are predicted and observed, respectively.

Once values for F_c have been estimated, they can be used in wall loss corrections to parametrize the growth of particles lost to the chamber walls. The change in the deposited particle number-size distribution also is governed by the the aerosol General Dynamic Equation, but only wall loss and condensation process affect the number-size

distribution:

$$\frac{\partial n_w\left(D_p, t\right)}{\partial t} = \beta\left(D_p\right) n_s\left(D_p, t\right) - F_c \varpi \left[-\frac{1}{D_p^2} n_w\left(D_p, t\right) + \frac{1}{D_p} \frac{\partial n_w\left(D_p, t\right)}{\partial D_p} \right] \tag{A15}$$

where $n_w\left(D_p, t\right)$ (cm^{-3}) is the deposited particle number-size distribution, and ϖ is a factor that describes the extent of condensation to deposited particles. ϖ has a value between 0 (no condensation to deposited particles) and 1 (condensation to deposited particles is the same as that to suspended particles). ϖ values of 0 and 1 correspond to the lower and upper limits of particle wall-loss corrections, respectively. The aerosol General Dynamic Equations for suspended and deposited particles are solved simultaneously between each time step using the previously determined value for F_c at that time step and a constant value for ϖ. In the current work, wall loss corrections were calculated with $\varpi = 0$ and $\varpi = 1$ to evaluate the limits of condensation behavior to deposited particles.

Supplementary material related to this article is available online at http://www.atmos-chem-phys-discuss.net/13/20677/2013/ acpd-13-20677-2013-supplement.pdf.

Acknowledgements. This work was supported by the Office of Science (Biological and Environmental Research), US Department of Energy Grant DE-SC 0006626 and National Science Foundation Grants AGS-1057183 and ATM-0650061. We thank ManNin Chan for experimental assistance and Aiko Matsunaga for information regarding Tenax tube preparation and sampling procedures. Christine Loza, Lindsay Yee, and Jill Craven were supported by National Science Foundation Graduate Research Fellowships. Manabu Shiraiwa was supported by the Japan Society for the Promotion of Science (JSPS) Postdoctoral Fellowship for Research Abroad.

References

Aiken, A. C., DeCarlo, P. F., Kroll, J. H., Worsnop, D. R., Huffman, J. A., Docherty, K. S., Ulbrich, I. M., Mohr, C., Kimmel, J. R., Sueper, D., Sun, Y., Zhang, Q., Trimborn, A., Northway, M., Ziemann, P. J., Canagaratna, M. R., Onasch, T. B., Alfarra, M. R., Prévôt, A. S. H., Dommen, J., Duplissy, J., Metzger, A., Baltensperger, U., and Jimenez, J. L.: O/C and OM/OC ratios of primary, secondary, and ambient organic aerosols with high-resolution time-of-flight aerosol mass spectrometry, Environ. Sci. Technol., 42, 4478–4485, doi:10.1021/es703009q, 2008. 20682

Allan, J. D., Delia, A. E., Coe, H., Bower, K. N., Alfarra, M. R., Jimenez, J. L., Middlebrook, A. M., Drewnick, F., Onasch, T. B., Canagaratna, M. R., Jayne, J. T., and Worsnop, D. R.: A generalised method for the extraction of chemically resolved mass spectra from Aerodyne aerosol mass spectrometer data, J. Aerosol Sci., 35, 909–922, doi:10.1016/j.jaerosci.2004.02.007, 2004. 20682

Atkinson, R. and Arey, J.: Atmospheric degradation of volatile organic compounds, Chem. Rev., 103, 4605–4638, doi:10.1021/cr0206420, 2003. 20679

Canagaratna, M., Jayne, J., Jimenez, J., Allan, J., Alfarra, M., Zhang, Q., Onasch, T., Drewnick, F., Coe, H., Middlebrook, A., Delia, A., Williams, L., Trimborn, A., Northway, M., DeCarlo, P., Kolb, C., Davidovits, P., and Worsnop, D.: Chemical and microphysical characterization of ambient aerosols with the Aerodyne aerosol mass spectrometer, Mass Spectrom. Rev., 26, 185–222, doi:10.1002/mas.20115, 2007. 20682

Cocker, D. R., Flagan, R. C., and Seinfeld, J. H.: State-of-the-art chamber facility for studying atmospheric aerosol chemistry, Environ. Sci. Technol., 35, 2594–2601, doi:10.1021/es0019169, 2001. 20680

Craven, J. S., Yee, L. D., Ng, N. L., Canagaratna, M. R., Loza, C. L., Schilling, K. A., Yatavelli, R. L. N., Thornton, J. A., Ziemann, P. J., Flagan, R. C., and Seinfeld, J. H.: Analysis of secondary organic aerosol formation and aging using positive matrix factorization of high-resolution aerosol mass spectra: application to the dodecane low-NO_x system, Atmos. Chem. Phys., 12, 11795–11817, doi:10.5194/acp-12-11795-2012, 2012. 20679, 20682

Crump, J. G. and Seinfeld, J. H.: Turbulent deposition and gravitational sedimentation of an aerosol in a vessel of arbitrary shape, J. Aerosol Sci., 12, 405–415, doi:10.1016/0021-8502(81)90036-7, 1981. 20704

DeCarlo, P. F., Kimmel, J. R., Trimborn, A., Northway, M. J., Jayne, J. T., Aiken, A. C., Gonin, M., Fuhrer, K., Horvath, T., Docherty, K. S., Worsnop, D. R., and Jimenez, J. L.: Field-deployable, high-resolution, time-of-flight aerosol mass spectrometer, Anal. Chem., 78, 8281–8289, doi:10.1021/ac061249n, 2006. 20682

Eddingsaas, N. C., Loza, C. L., Yee, L. D., Chan, M., Schilling, K. A., Chhabra, P. S., Seinfeld, J. H., and Wennberg, P. O.: α-pinene photooxidation under controlled chemical conditions – Part 2: SOA yield and composition in low- and high-NO_x environments, Atmos. Chem. Phys., 12, 7413–7427, doi:10.5194/acp-12-7413-2012, 2012. 20690

Farmer, D. K., Matsunaga, A., Docherty, K. S., Surratt, J. D., Seinfeld, J. H., Ziemann, P. J., and Jimenez, J. L.: Response of an aerosol mass spectrometer to organonitrates and organosulfates and implications for atmospheric chemistry, P. Natl. Acad. Sci. USA, 107, 6670–6675, doi:10.1073/pnas.0912340107, 2010. 20694

Francisco, M. A. and Krylowski, J.: Chemistry of organic nitrates: Thermal chemistry of linear and branched organic nitrates, Ind. Eng. Chem. Res., 44, 5439–5446, doi:10.1021/ie049380d, 2005. 20694

Fraser, M. P., Cass, G. R., Simoneit, B. R. T., and Rasmussen, R. A.: Air quality model evaluation data for organics. 4. C_2–C_{36} non-aromatic hydrocarbons, Environ. Sci. Technol., 31, 2356–2367, doi:10.1021/es960980g, 1997. 20678

Gentner, D. R., Isaacman, G., Worton, D. R., Chan, A. W. H., Dallmann, T. R., Davis, L., Liu, S., Day, D. A., Russell, L. M., Wilson, K. R., Weber, R., Guha, A., Harley, R. A., and Goldstein, A. H.: Elucidating secondary organic aerosol from diesel and gasoline vehicles through detailed characterization of organic carbon emissions, P. Natl. Acad. Sci. USA, 109, 18318–18323, doi:10.1073/pnas.1212272109, 2012. 20678, 20700

Hildebrandt, L., Donahue, N. M., and Pandis, S. N.: High formation of secondary organic aerosol from the photo-oxidation of toluene, Atmos. Chem. Phys., 9, 2973–2986, doi:10.5194/acp-9-2973-2009, 2009. 20685

Jenkin, M. E., Saunders, S. M., Wagner, V., and Pilling, M. J.: Protocol for the development of the Master Chemical Mechanism, MCM v3 (Part B): tropospheric degradation of aromatic volatile organic compounds, Atmos. Chem. Phys., 3, 181–193, doi:10.5194/acp-3-181-2003, 2003. 20696

Jordan, C. E., Ziemann, P. J., Griffin, R. J., Lim, Y. B., Atkinson, R., and Arey, J.: Modeling SOA formation from OH reactions with C_8–C_{17} *n*-alkanes, Atmos. Environ., 42, 8015–8026, doi:10.1016/j.atmosenv.2008.06.017, 2008. 20684, 20696, 20714

Keywood, M. D., Varutbangkul, V., Bahreini, R., Flagan, R. C., and Seinfeld, J. H.: Secondary organic aerosol formation from the ozonolysis of cycloalkenes and related compounds, Environ. Sci. Technol., 38, 4157–4164, doi:10.1021/es035363o, 2004. 20680, 20704

Kroll, J. H., Donahue, N. M., Jimenez, J. L., Kessler, S. H., Canagaratna, M. R., Wilson, K. R., Altieri, K. E., Mazzoleni, L. R., Wozniak, A. S., Bluhm, H., Mysak, E. R., Smith, J. D., Kolb, C. E., and Worsnop, D. R.: Carbon oxidation state as a metric for describing the chemistry of atmospheric organic aerosol, Nat. Chem., 3, 133–139, doi:10.1038/NCHEM.948, 2011. 20694

Kwok, E. S. and Atkinson, R.: Estimation of hydroxyl radical reaction rate constants for gas-phase organic compounds using a structure–reactivity relationship: an update, Atmos. Environ., 29, 1685–1695, doi:10.1016/1352-2310(95)00069-B, 1995. 20683

Lambe, A. T., Onasch, T. B., Croasdale, D. R., Wright, J. P., Martin, A. T., Franklin, J. P., Massoli, P., Kroll, J. H., Canagaratna, M. R., Brune, W. H., Worsnop, D. R., and Davidovits, P.: Transitions from functionalization to fragmentation reactions of laboratory secondary organic aerosol (SOA) generated from the OH oxidation of alkane precursors, Environ. Sci. Technol., 46, 5430–5437, doi:10.1021/es300274t, 2012. 20679, 20690, 20691, 20695, 20699

Lim, Y. B. and Ziemann, P. J.: Products and mechanism of secondary organic aerosol formation from reactions of *n*-alkanes with OH radicals in the presence of NO_x, Environ. Sci. Technol., 39, 9229–9236, doi:10.1021/es051447g, 2005. 20679, 20694

Lim, Y. B. and Ziemann, P. J.: Chemistry of secondary organic aerosol formation from OH radical-initiated reactions of linear, branched, and cyclic alkanes in the presence of NO_x, Aerosol Sci. Tech., 43, 604–619, doi:10.1080/02786820902802567, 2009a. 20679, 20691

Lim, Y. B. and Ziemann, P. J.: Effects of molecular structure on aerosol yields from OH radical-initiated reactions of linear, branched, and cyclic alkanes in the presence of NO_x, Environ. Sci. Technol., 43, 2328–2334, doi:10.1021/es803389s, 2009b. 20679, 20687, 20688, 20700

Lim, Y. B. and Ziemann, P. J.: Kinetics of the heterogeneous conversion of 1,4-hydroxycarbonyls to cyclic hemiacetals and dihydrofurans on organic aerosol particles, Phys. Chem. Chem. Phys., 11, 8029–8039, doi:10.1039/B904333K, 2009c. 20679

Loza, C. L., Chhabra, P. S., Yee, L. D., Craven, J. S., Flagan, R. C., and Seinfeld, J. H.: Chemical aging of *m*-xylene secondary organic aerosol: laboratory chamber study, Atmos. Chem. Phys., 12, 151–167, doi:10.5194/acp-12-151-2012, 2012. 20685, 20695, 20704

Martin, P., Tuazon, E. C., Aschmann, S. M., Arey, J., and Atkinson, R.: Formation and atmospheric reactions of 4,5-dihydro-2-methylfuran, J. Phys. Chem. A, 106, 11492–11501, doi:10.1021/jp021499h, 2002. 20684

Matsunaga, A. and Ziemann, P. J.: Gas-wall partitioning of organic compounds in a Teflon film chamber and potential effects on reaction product and aerosol yield measurements, Aerosol Sci. Tech., 44, 881–892, doi:10.1080/02786826.2010.501044, 2010. 20685, 20692, 20693

McMurry, P. H. and Rader, D. J.: Aerosol wall losses in electrically charged chambers, Aerosol Sci. Tech., 4, 249–268, doi:10.1080/02786828508959054, 1985. 20704

Molina, L. T., Madronich, S., Gaffney, J. S., Apel, E., de Foy, B., Fast, J., Ferrare, R., Herndon, S., Jimenez, J. L., Lamb, B., Osornio-Vargas, A. R., Russell, P., Schauer, J. J., Stevens, P. S., Volkamer, R., and Zavala, M.: An overview of the MILAGRO 2006 Campaign: Mexico City emissions and their transport and transformation, Atmos. Chem. Phys., 10, 8697–8760, doi:10.5194/acp-10-8697-2010, 2010. 20684

Ng, N. L., Chhabra, P. S., Chan, A. W. H., Surratt, J. D., Kroll, J. H., Kwan, A. J., McCabe, D. C., Wennberg, P. O., Sorooshian, A., Murphy, S. M., Dalleska, N. F., Flagan, R. C., and Seinfeld, J. H.: Effect of NO_x level on secondary organic aerosol (SOA) formation from the photooxidation of terpenes, Atmos. Chem. Phys., 7, 5159–5174, doi:10.5194/acp-7-5159-2007, 2007a. 20688, 20690

Ng, N. L., Kroll, J. H., Chan, A. W. H., Chhabra, P. S., Flagan, R. C., and Seinfeld, J. H.: Secondary organic aerosol formation from *m*-xylene, toluene, and benzene, Atmos. Chem. Phys., 7, 3909–3922, doi:10.5194/acp-7-3909-2007, 2007b. 20704

Perraud, V., Bruns, E. A., Ezell, M. J., Johnson, S. N., Yu, Y., Alexander, M. L., Zelenyuk, A., Imre, D., Chang, W. L., Dabdub, D., Pankow, J. F., and Finlayson-Pitts, B. J.: Nonequilibrium atmospheric secondary organic aerosol formation and growth, P. Natl. Acad. Sci. USA, 109, 2836–2841, doi:10.1073/pnas.1119909109, 2012. 20691

Pierce, J. R., Engelhart, G. J., Hildebrandt, L., Weitkamp, E. A., Pathak, R. K., Donahue, N. M., Robinson, A. L., Adams, P. J., and Pandis, S. N.: Constraining particle evolution from wall losses, coagulation, and condensation-evaporation in smog-chamber experiments: optimal estimation based on size distribution measurements, Aerosol Sci. Tech., 42, 1001–1015, doi:10.1080/02786820802389251, 2008. 20685, 20701, 20704

Presto, A. A., Miracolo, M. A., Kroll, J. H., Worsnop, D. R., Robinson, A. L., and Donahue, N. M.: Intermediate-volatility organic compounds: a potential source of ambient oxidized organic aerosol, Environ. Sci. Technol., 43, 4744–4749, doi:10.1021/es803219q, 2009. 20696

Presto, A. A., Miracolo, M. A., Donahue, N. M., and Robinson, A. L.: Secondary organic aerosol formation from high-NO_x photo-oxidation of low volatility precursors: *n*-alkanes, Environ. Sci. Technol., 44, 2029–2034, doi:10.1021/es903712r, 2010. 20679, 20688, 20689

Riipinen, I., Pierce, J. R., Yli-Juuti, T., Nieminen, T., Häkkinen, S., Ehn, M., Junninen, H., Lehtipalo, K., Petäjä, T., Slowik, J., Chang, R., Shantz, N. C., Abbatt, J., Leaitch, W. R., Kerminen, V.-M., Worsnop, D. R., Pandis, S. N., Donahue, N. M., and Kulmala, M.: Organic condensation: a vital link connecting aerosol formation to cloud condensation nuclei (CCN) concentrations, Atmos. Chem. Phys., 11, 3865–3878, doi:10.5194/acp-11-3865-2011, 2011. 20691

Rogge, W. F., Hildemann, L. M., Mazurek, M. A., Cass, G. R., and Simoneit, B. R. T.: Sources of fine organic aerosol. 3. Road dust, tire debris, and organometallic brake lining dust: roads as sources and sinks, Environ. Sci. Technol., 27, 1892–1904, doi:10.1021/es00046a019, 1993. 20678

Saunders, S. M., Jenkin, M. E., Derwent, R. G., and Pilling, M. J.: Protocol for the development of the Master Chemical Mechanism, MCM v3 (Part A): tropospheric degradation of non-aromatic volatile organic compounds, Atmos. Chem. Phys., 3, 161–180, doi:10.5194/acp-3-161-2003, 2003. 20696

Schauer, J. J., Kleeman, M. J., Cass, G. R., and Simoneit, B. R. T.: Measurement of emissions from air pollution sources. 2. C_1 through C_{30} organic compounds from medium duty diesel trucks, Environ. Sci. Technol., 33, 1578–1587, doi:10.1021/es980081n, 1999. 20678

Schauer, J. J., Kleeman, M. J., Cass, G. R., and Simoneit, B. R. T.: Measurement of emissions from air pollution sources. 5. C_1–C_{32} organic compounds from gasoline-powered motor vehicles, Environ. Sci. Technol., 36, 1169–1180, doi:10.1021/es0108077, 2002. 20678

Seinfeld, J. H. and Pandis, S. N.: Atmospheric Chemistry and Physics, 2nd edn., John Wiley and Sons, Inc., Hoboken, NJ, 2006. 20679, 20701, 20702

Shilling, J. E., Chen, Q., King, S. M., Rosenoern, T., Kroll, J. H., Worsnop, D. R., DeCarlo, P. F., Aiken, A. C., Sueper, D., Jimenez, J. L., and Martin, S. T.: Loading-dependent elemental composition of α-pinene SOA particles, Atmos. Chem. Phys., 9, 771–782, doi:10.5194/acp-9-771-2009, 2009. 20695

Shiraiwa, M. and Seinfeld, J. H.: Equilibration timescale of atmospheric secondary organic aerosol partitioning, Geophys. Res. Lett., 39, L24801, doi:10.1029/2012GL054008, 2012. 20691

Shiraiwa, M., Pfrang, C., Koop, T., and Pöschl, U.: Kinetic multi-layer model of gas-particle interactions in aerosols and clouds (KM-GAP): linking condensation, evaporation and chemical reactions of organics, oxidants and water, Atmos. Chem. Phys., 12, 2777–2794, doi:10.5194/acp-12-2777-2012, 2012. 20691

Shiraiwa, M., Yee, L. D., Schilling, K. A., Loza, C. L., Craven, J. S., Zuend, A., Ziemann, P. J., and Seinfeld, J. H.: Size distribution dynamics reveal particle-phase chemistry in organic aerosol formation, P. Natl. Acad. Sci. USA, 110, 11746–11750, doi:10.1073/pnas.1307501110, 2013TS2, 15, 17, 19, 23. 20691, 20693, 20695, 20699

Song, C., Na, K., and Cocker, D. R.: Impact of the hydrocarbon to NO_x ratio on secondary organic aerosol formation, Environ. Sci. Technol., 39, 3143–3149, doi:10.1021/es0493244, 2005. 20690

Stephens, S., Madronich, S., Wu, F., Olson, J. B., Ramos, R., Retama, A., and Muñoz, R.: Weekly patterns of México City's surface concentrations of CO, NO_x, PM_{10} and O_3 during 1986–2007, Atmos. Chem. Phys., 8, 5313–5325, doi:10.5194/acp-8-5313-2008, 2008. 20684

Tkacik, D. S., Presto, A. A., Donahue, N. M., and Robinson, A. L.: Secondary organic aerosol formation from intermediate-volatility organic compounds: cyclic, linear, and branched alkanes, Environ. Sci. Technol., 46, 8773–8781, doi:10.1021/es301112c, 2012. 20679, 20687, 20689

Verheggen, B. and Mozurkewich, M.: An inverse modeling procedure to determine particle growth and nucleation rates from measured aerosol size distributions, Atmos. Chem. Phys., 6, 2927–2942, doi:10.5194/acp-6-2927-2006, 2006. 20703

Volkamer, R., Sheehy, P., Molina, L. T., and Molina, M. J.: Oxidative capacity of the Mexico City atmosphere – Part 1: A radical source perspective, Atmos. Chem. Phys., 10, 6969–6991, doi:10.5194/acp-10-6969-2010, 2010. 20684

Weitkamp, E. A., Sage, A. M., Pierce, J. R., Donahue, N. M., and Robinson, A. L.: Organic aerosol formation from photochemical oxidation of diesel exhaust in a smog chamber, Environ. Sci. Technol., 41, 6969–6975, doi:10.1021/es070193r, 2007. 20685

Yee, L. D., Craven, J. S., Loza, C. L., Schilling, K. A., Ng, N. L., Canagaratna, M. R., Ziemann, P. J., Flagan, R. C., and Seinfeld, J. H.: Secondary organic aerosol formation from low-NO_x photooxidation of dodecane: evolution of multigeneration gas-phase chemistry and aerosol composition, J. Phys. Chem. A, 116, 6211–6230, doi:10.1021/jp211531h, 2012. 20679, 20682, 20695, 20696, 20698, 20699

Yee, L. D., Craven, J. S., Loza, C. L., Schilling, K. A., Ng, N. L., Canagaratna, M. R., Ziemann, P. J., Flagan, R. C., and Seinfeld, J. H.: Effect of chemical structure on secondary organic aerosol formation from C_{12} alkanes, Atmos. Chem. Phys. Discuss., 13, 10859–10903, doi:10.5194/acpd-13-10859-2013, 2013. 20679, 20695, 20698, 20699

Table 1. SOA precursor and aerosol properties.

Alkane	Structure	$k_{OH} \times 10^{12\,a}$ ($cm^3\,s^{-1}$)	High-NO_x density ($g\,cm^{-3}$)	Low-NO_x density ($g\,cm^{-3}$)
n-Dodecane (Dod)	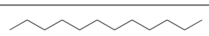	13.9[b]	1.28 ± 0.01	1.12 ± 0.03
2-Methylundecane (Mud)	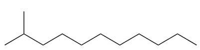	13.1 ± 0.7	1.28 ± 0.01	1.12 ± 0.03
Hexylcyclohexane (Hch)	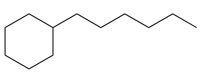	17.4 ± 0.6	1.29 ± 0.01	1.17 ± 0.03
Cyclododecane (Cdd)	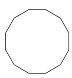	14.7 ± 0.4	1.23 ± 0.02	1.28 ± 0.03

[a] Calculated from a relative rate experiment at 297 K.
[b] Jordan et al. (2008) for 298 K.

Table 2. High-NO_x experimental details.

Expt.[a]	Alkane	Seed vol. ($\mu m^3\,cm^{-3}$)	NO_o (ppbv)	$NO_{2,o}$ (ppbv)	HC_o (ppbv)
MH1	Mud	31.7 ± 9.5	94.1 ± 0.5	6.6 ± 0.2	11.6 ± 0.4
MH2	Mud	41.6 ± 12.5	97.7 ± 0.5	5.8 ± 0.2	79.6 ± 2.5
DH1	Dod	30.9 ± 9.3	93.8 ± 0.5	6.3 ± 0.2	9.7 ± 0.3
DH2	Dod	26.1 ± 7.8	96.8 ± 0.5	7.1 ± 0.2	59.2 ± 1.9
DH3	Dod	30.4 ± 9.1	96.5 ± 0.5	6.1 ± 0.2	63.6 ± 2.0
HH1	Hch	34.1 ± 10.2	101 ± 0.5	2.6 ± 0.2	11.5 ± 0.4
HH2	Hch	40.0 ± 12.0	95.4 ± 0.5	2.9 ± 0.2	65.0 ± 2.1
CH1	Cdd	38.7 ± 11.6	95.6 ± 0.5	6.8 ± 0.2	8.5 ± 0.3
CH2	Cdd	37.7 ± 11.3	93.4 ± 0.5	7.9 ± 0.2	61.0 ± 2.0

[a] The first letter of each experiment identifier refers to the alkane, and the second letter refers to high- (H) or low- (L) NO_x conditions.

Table 2. Continued.

Expt.[a]	ΔHC (ppbv)	ΔM_o^b ($\mu g\,m^{-3}$)	Yield[b] (frac.)
MH1	11.6	8.5–16.8	0.11–0.214
MH2	79.1	104–195	0.190–0.357
DH1	9.2	19.4–39.5	0.303–0.617
DH2	56.8	91.3–212	0.234–0.542
DH3	61.2	103–214	0.224–0.508
HH1	11.5	26.8–45.0	0.340–0.572
HH2	64.9	205–270	0.458–0.605
CH1	8.5	55.5–90.8	0.98–1.6
CH2	58.6	320–398	0.801–1.00

[a] The first letter of each experiment identifier refers to the alkane, and the second letter refers to high- (H) or low- (L) NO_x conditions.

[b] The range of values listed correspond to the two limiting assumptions for suspended vapor-deposited particle gas-particle partitioning. The smaller and larger values correspond to the upper and lower partitioning limits, respectively.

Table 3. Low-NO_x experimental details.

Expt.[a]	Alkane	Seed vol. ($\mu m^3 cm^{-3}$)	HC_o (ppbv)	ΔHC (ppbv)	ΔM_o^b ($\mu g m^{-3}$)	Yield[b] (frac.)
ML1	Mud	21.8 ± 6.5	8.5 ± 0.3	8.4	7.9–15.4	0.14–0.27
ML2[c]	Mud	16.7 ± 5.0	28.9 ± 0.9	28.1	27.5–57.6	0.148–0.310
ML3	Mud	15.9 ± 4.8	40.2 ± 1.3	38.1	49.2–86.4	0.185–0.325
DL1	Dod	16.7 ± 5.0	8.2 ± 0.3	7.9	1.8–4.2	0.033–0.078
DL2[c]	Dod	12.1 ± 3.6	34.0 ± 1.1	33.6	35.1–64.9	0.149–0.275
HL1[c]	Hch	11.2 ± 3.4	15.6 ± 0.5	15.5	32.9–70.2	0.304–0.649
HL2	Hch	20.0 ± 6	41.3 ± 1.3	40.8	98.7–121	0.354–0.435
CL1	Cdd	18.9 ± 5.7	3.5 ± 0.1	3.4	4.9–10.6	0.22–0.46
CL2[c]	Cdd	15.3 ± 4.6	10.4 ± 0.3	10.3	29.9–61.7	0.424–0.875
CL3	Cdd	21.5 ± 6.5	46.6 ± 1.5	45.1	195–229	0.611–0.727

[a] The first letter of each experiment identifier refers to the alkane, and the second letter refers to high- (H) or low- (L) NO_x conditions.
[b] The range of values listed corresponds to the two limiting assumptions for suspended vapor-deposited particle gas-particle partitioning. The smaller and larger values correspond to the upper and lower partitioning limits, respectively.
[c] Due to chamber volume limitations, these experiments were run in two parts. The initial conditions for the two separate experiments are listed Table S2.

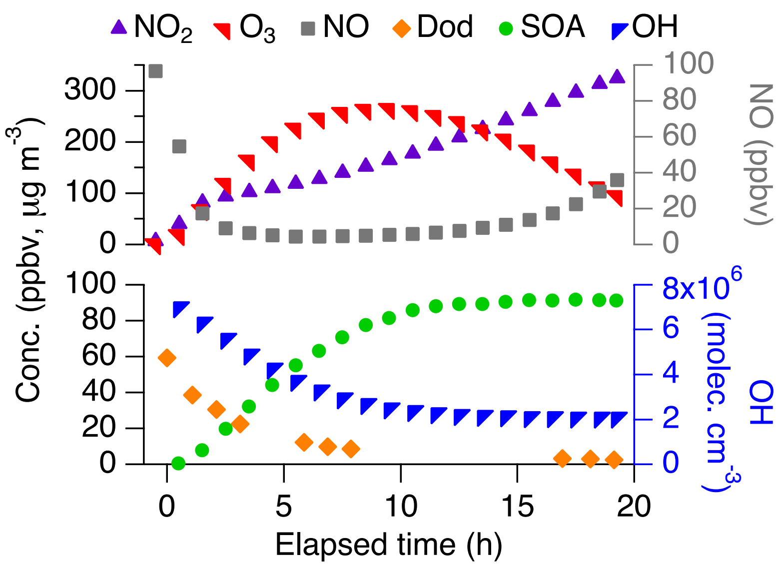

Fig. 1. Temporal trends of gas-phase species and SOA mass concentration during a typical high-NO_x experiment. On the left axis, SOA mass concentration (lower limit) is reported in $\mu g m^{-3}$, and dodecane, O_3, and NO_2 concentrations are reported in ppbv. NO and OH concentrations are given on the right axis. NO_2, O_3, NO, SOA mass, and OH concentrations are hourly averaged. Data are shown for the 57 ppbv dodecane experiment, DH2 (see Table 2). OH concentration was calculated from the dodecane decay.

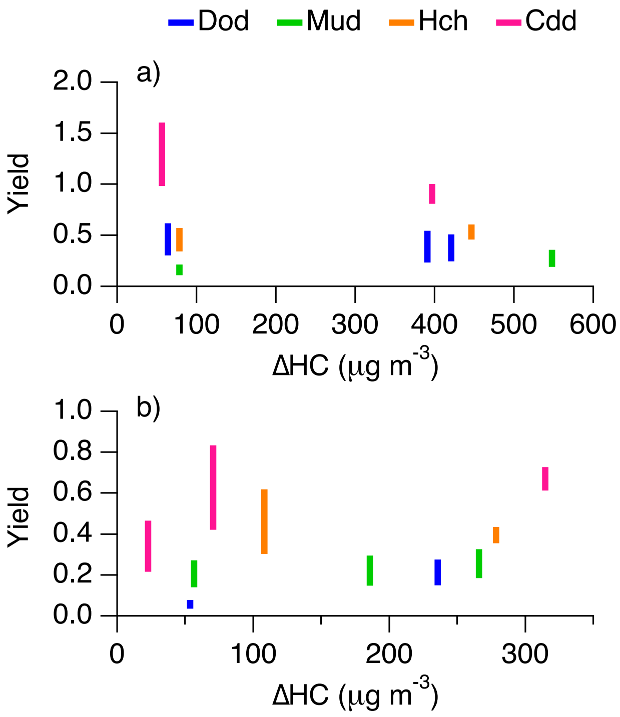

Fig. 2. SOA yield at 95–100 % of initial hydrocarbon reacted under **(a)** high- and **(b)** low-NO_x conditions. Each line shows the range between the lower limit (deposited particles do not undergo gas-particle partitioning) and upper limit (gas-particle partitioning to deposited particles is that same as that to suspended particles) SOA yields for an experiment.

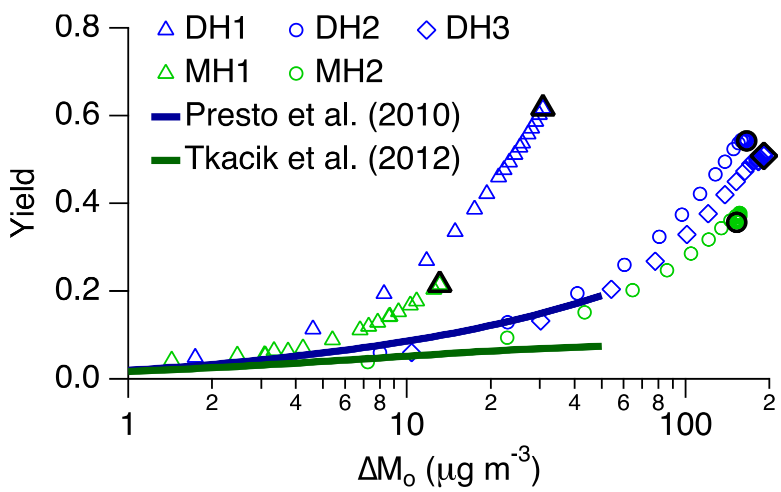

Fig. 3. Comparison of SOA yields as a function of organic aerosol mass concentration, ΔM_o, observed in the present study with those reported in previous studies. For the present study, final yields (after 95–100 % alkane reacted) are denoted by the black markers.

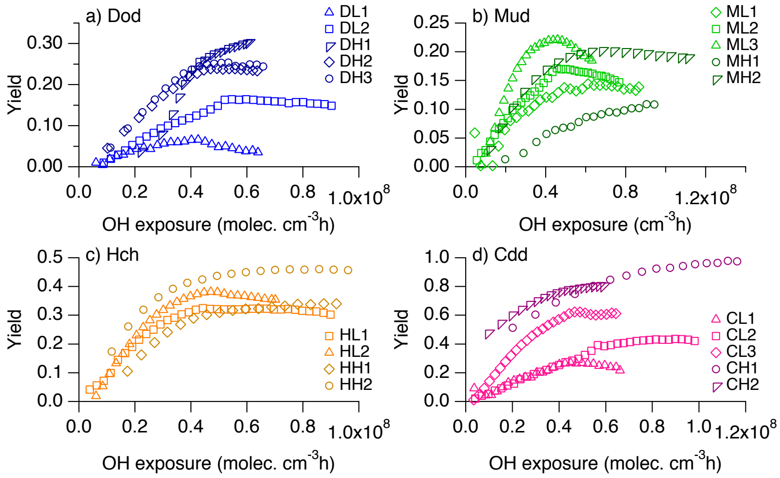

Fig. 4. Comparison of lower limit case SOA yields under high- and low-NO_x conditions for **(a)** dodecane, **(b)** 2-methylundecane, **(c)** hexylcyclohexane, and **(d)** cyclododecane. The second letter in each experiment identifier corresponds to the NO_x conditions (H for high, L for low) and increasing numbers correspond to increasing initial alkane concentrations (see Tables 2 and 3).

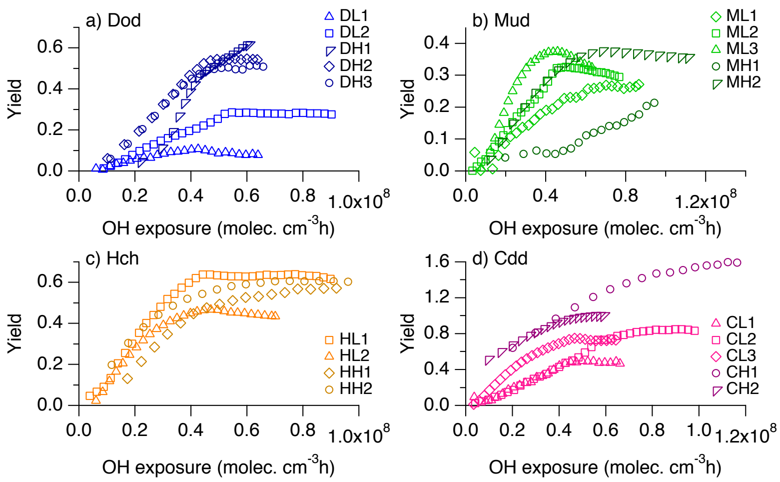

Fig. 5. Comparison of upper limit case SOA yields under high- and low-NO_x conditions for **(a)** dodecane, **(b)** 2-methylundecane, **(c)** hexylcyclohexane, and **(d)** cyclododecane. The second letter in each experiment identifier corresponds to the NO_x conditions (H for high, L for low) and increasing numbers correspond to increasing initial alkane concentrations (see Tables 2 and 3).

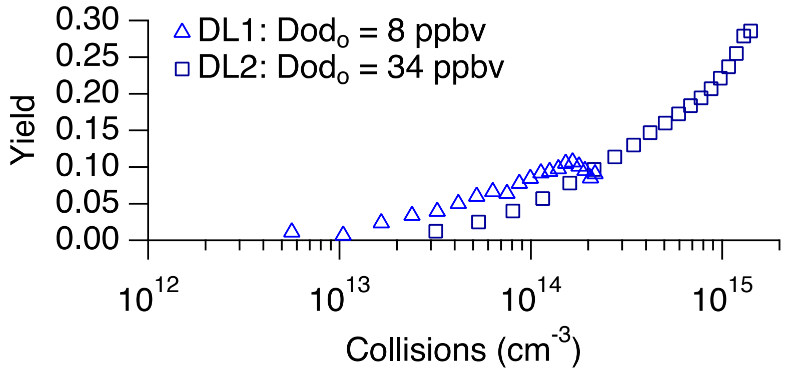

Fig. 6. SOA yield (upper limit) as a function of estimated cumulative SVOC-particle collisions per unit chamber volume for low-NO_x dodecane photooxidation experiments.

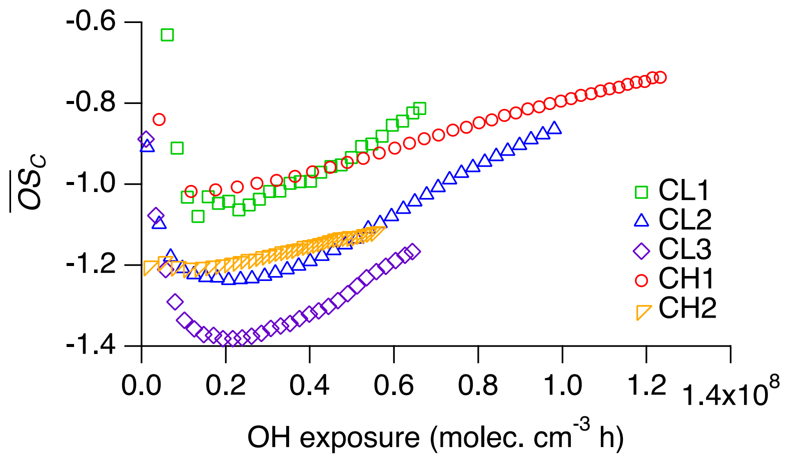

Fig. 7. SOA average carbon oxidation state as a function of OH exposure for high- and low-NO_x cyclododecane photooxidation.

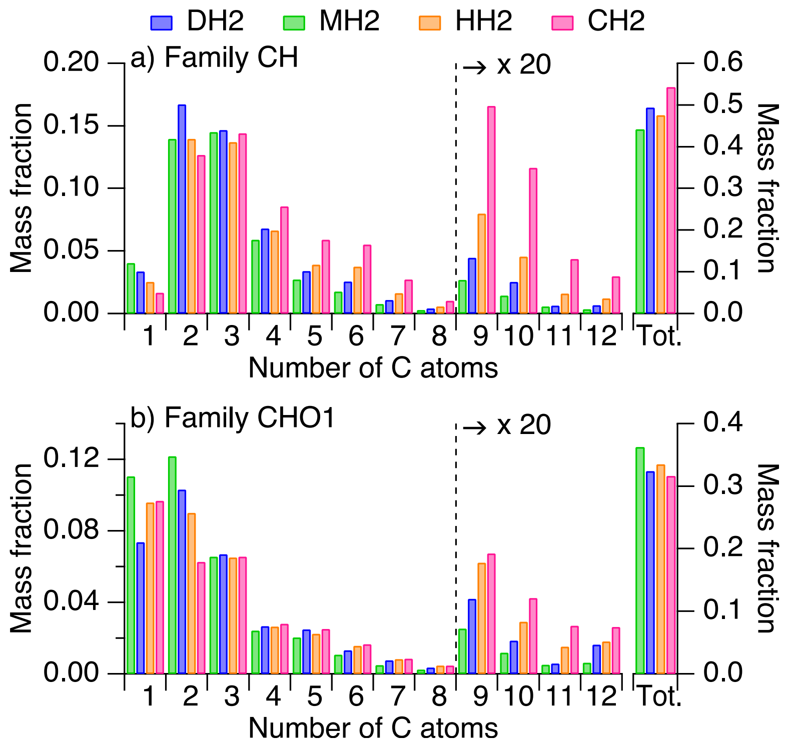

Fig. 8. Contribution of ions detected in the AMS to the bulk organic mass concentration for high-NO_x alkane photooxidation. Ions are grouped into families according to the ion atomic composition and displayed as a function of carbon atoms in the ion. Tot. is the sum over all carbon atom numbers for each family. The data represent a 30 min average of the SOA formed after 95–100 % of the initial alkane had reacted.

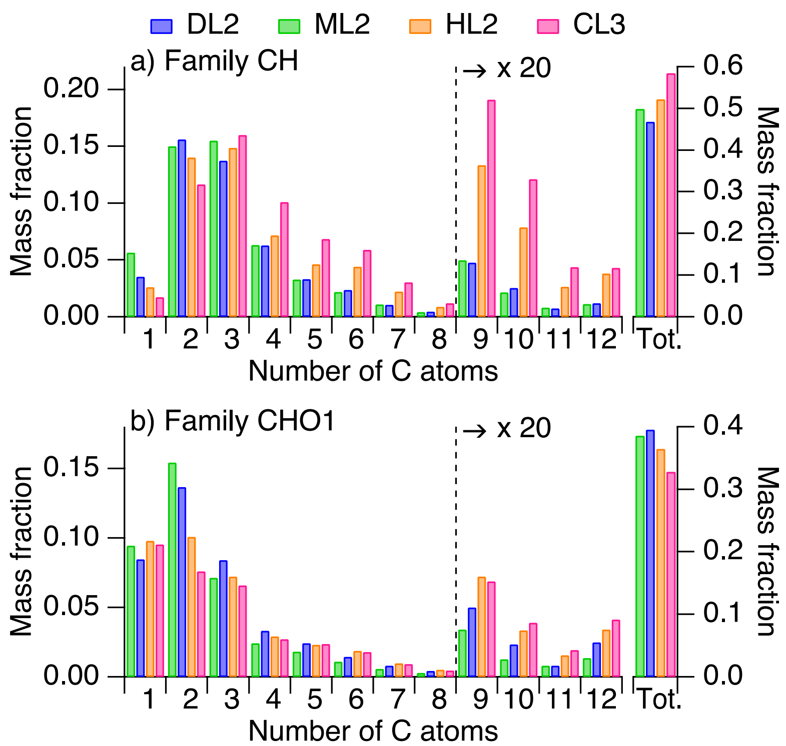

Fig. 9. Contribution of ions detected in the AMS to the bulk organic mass concentration for low-NO_x alkane photooxidation. Ions are grouped into families according to the ion atomic composition and displayed as a function of carbon atoms in the ion. Tot. is the sum over all carbon atom numbers for each family. The data represent a 60 min average of the SOA formed after 95–100 % of the initial alkane had reacted.

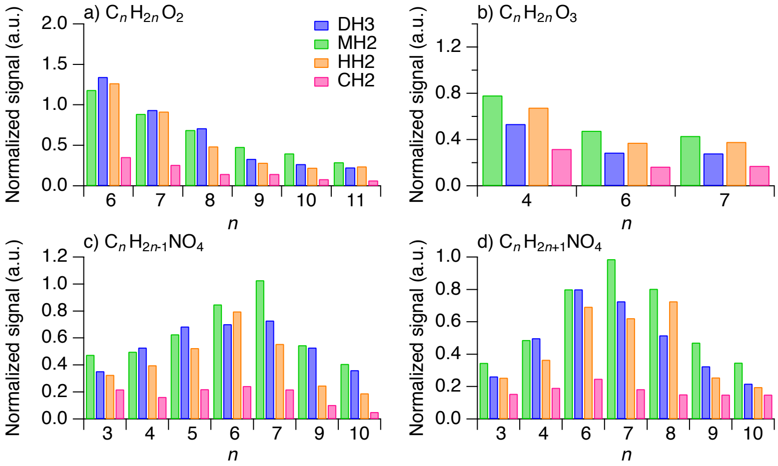

Fig. 10. Comparison of gas-phase fragmentation reaction products from high-NO_x alkane photooxidation measured by the CIMS. The signal is normalized by the concentration of alkane reacted. All molecular formulae are proposed assignments. The data represent a 30 min average of gas-phase species after 95–100 % of the initial alkane had reacted. The ions monitored and their proposed chemical assignments are given in Table S3.